Supplementary Information (SI) for Materials Horizons.
This journal is © The Royal Society of Chemistry 2025

Supporting Information

Multi-functional smart bulk hydrogel panels with strong Near-infrared shielding and active local control

Yitong Ding[a, b], *Gang Li*[c], *Keunhyuk Ryu*[d], *JianGuo Guan*[c], *Shancheng Wang*[d], *Ying Xiong*[b, *], *Shaoyun Guo*[b], *Yi Long*[d, *]

[a] Key Laboratory of Biobased Polymer Materials, Shandong Provincial Education Department, College of Polymer Science and Engineering, Qingdao University of Science and Technology, Qingdao, China.

[b] State Key Laboratory of Polymer Materials Engineering, Sichuan Provincial Engineering Laboratory of Plastic/Rubber Complex Processing Technology, Polymer Research Institute of Sichuan University, Chengdu 610065, China.

[c] State Key Laboratory of Advanced Technology for Materials Synthesis and Processing, International School of Materials Science and Engineering, Wuhan University of Technology, Wuhan 430070, China.

[d] Department of Electronic Engineering, The Chinese University of Hong Kong, Shatin, New Territories, Hong Kong SAR 999077, China.

* Corresponding author. Email: xiongying@scu.edu.cn (Ying Xiong).

* Corresponding author. Email: yilong@cuhk.edu.hk (Yi Long).

Experimental Section

Characterization

The UV-Vis-NIR spectra for the sample were measured with the UV-Vis-NIR spectrophotometer system with the integration sphere attached (Avantes AvaSpec-ULS2048L StarLine Versatile Fiber-optic Spectrometer and AvaSpec-NIR256–2.5-HSC-EVO). The spectrophotometer is equipped with a heating and cooling stage (Linkam PE120) to control the sample temperature. The luminous (T_{lum}, 380-780 nm), NIR (T_{NIR}, 780-2500 nm), solar (T_{sol}, 280-2500 nm) transmittance and the luminous (R_{lum}, 380-780 nm), NIR (R_{NIR}, 780-2500 nm), solar (R_{sol}, 280-2500 nm) reflectance were calculated using the method in the published work (Equation S1 and Equation S2) [1, 2].

$$T_{lum/NIR/sol} = \frac{\int \varphi_{lum/IR/sol}(\lambda)T(\lambda)d\lambda}{\int \varphi_{lum/IR/sol}(\lambda)d\lambda} \quad (1)$$

$$R_{lum/NIR/sol} = \frac{\int \varphi_{lum/IR/sol}(\lambda)R(\lambda)d\lambda}{\int \varphi_{lum/IR/sol}(\lambda)d\lambda} \quad (2)$$

Wherein, $T(\lambda)$ and $R(\lambda)$ denoted the spectral transmittance and reflectance, φ_{lum} is the standard luminous efficiency function of photopic vision in the wavelength range of 380-780 nm, and $\varphi_{IR/solar}$ is the IR/solar irradiance spectra for air mass 1.5.

Scanning electron microscopy (SEM, JSM5900LV, Japan Electronics Co., Ltd.) and nano-measurer software were used to observe and analyze the microscopic morphology of photothermal films and post-phase transition gels (equilibrated at 60 °C for 15 min, rapidly cooled in liquid nitrogen and freeze-dried for 12 h). X-Ray Spectroscopy (EDS) was used to characterize the species and distribution of elements on the surface of the photothermal films.

An infrared thermal imaging camera (Flir T620) was used to determine the near-infrared photothermal capabilities of different photothermal films and gel panels. The thermal imaging camera and laser were placed on the same side of the samples, and the photothermal capacity of the photothermal film and gel panels were recorded at different powers. Meanwhile, the laser power meter was placed on the other side of the samples to compare the dynamic modulation of modified gel panels in different phase transition states.

The relative transmittance of different modified gels was measured in real-time using a spectrometer (MAYA, Ocean optics, USA).

The emissivity curve of 2.5-25 μm was collected on an FTIR spectrometer (Perkin Elmer Frontier) with an integrating sphere attached[3, 4].

$$\varepsilon(T,\lambda) = A(T,\lambda) = 1 - T(T,\lambda) - R(T,\lambda) \tag{3}$$

$$\varepsilon = \frac{\int_{2.5\ \mu m}^{25\ \mu m} I_{BB}(T,\lambda)\varepsilon(T,\lambda)d\lambda}{\int_{2.5\ \mu m}^{25\ \mu m} I_{BB}(T,\lambda)d\lambda} \tag{4}$$

$$I_{BB}(T,\lambda) = \frac{2hc^2}{\lambda^5} * \frac{1}{e^{\frac{hc}{\lambda kT}} - 1} \tag{5}$$

Wherein, $A(T,\lambda)$ is the absorbance of different hydrogel panels, $I_{BB}(T,\lambda)$ is the intensity of radiation from an ideal blackbody at temperature (T) (Planck's law), h is Planck's constant, 6.626×10^{-34} $m^2\cdot kg/s$, c is the speed of light, 2.998×10^{8} m/s, k is the Boltzmann constant, 1.380649×10^{-23} J/K, e is the base of the natural logarithm, 2.71828, and λ is the wavelength of light.

The images and videos of different gel panels were obtained using a Canon M5 camera.

EnergyPlus software was used to simulate building energy consumption. A building model with the dimensions of 8 m in length, 6 m in width and 2.7 m in height was employed. And four windows with the dimension of 3 m in width and 2 m in height were installed in the four orientations to avoid the influence of orientation. The boundary conditions for heating and cooling were 18 °C and 26 °C, respectively. The optical properties of different windows were listed in Table S1. The hourly weather data for a Typical Meteorological Year (TMY) of Singapore and Bangkok were used in this simulation[2].

The thermal transmission coefficient (U-value) and solar heat gain coefficient (SHGC-value) were calculated to compare the thermal and optical properties of different windows[5, 6].

$$R = \frac{d}{\lambda} \tag{6}$$

$$U = \frac{1}{R_i + R_e + \sum R_{be}} \tag{7}$$

Wherein, d is the thickness (Table S2), λ is the thermal conductivity, R is the thermal resistance, R_i and R_e are thermal resistance of internal surface and external surface, respectively, R_{be} is the thermal resistance of the window components, U is the U-value (thermal transmission coefficient).

$$SHGC = \frac{\sum g_g * A_g + \sum g_f * A_f}{A_w} \quad (8)$$

Wherein, $SHGC$ is the solar heat gain coefficient, g_g and g_f are the individual total solar transmittance values of the glass and frame respectively, A_g and A_f are the areas of glass and frame respectively, A_w is the window total area.

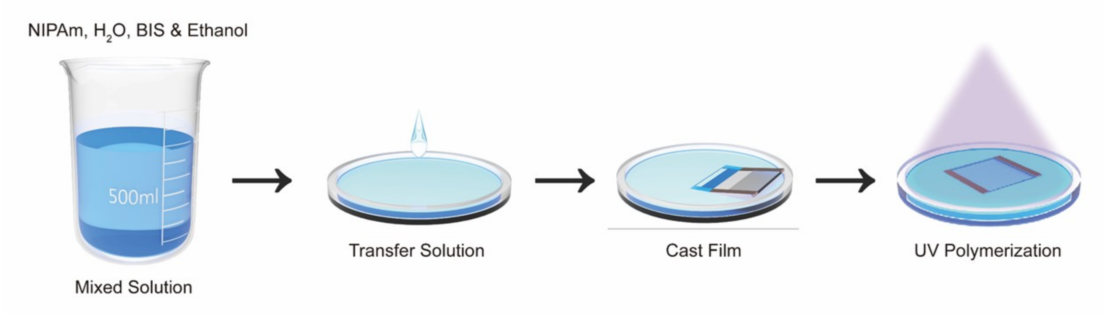

Fig. S1. Fabrication process of gel panels.

Fig. S2. Optical photographs of (A) bulk hydrogels and (B) microgel.

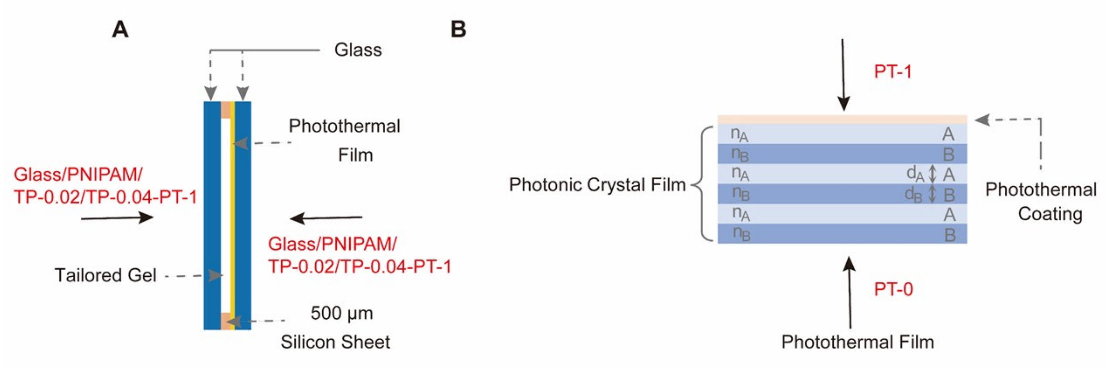

Fig. S3. (A) Schematic diagrams of the gel panels and (B) composite photothermal film (PT film). "-0" and "-1" represent different surfaces of the photothermal film, respectively. "-0" represent the direction of the photonic crystal layer. "-1" represent direction of the photothermal coating.

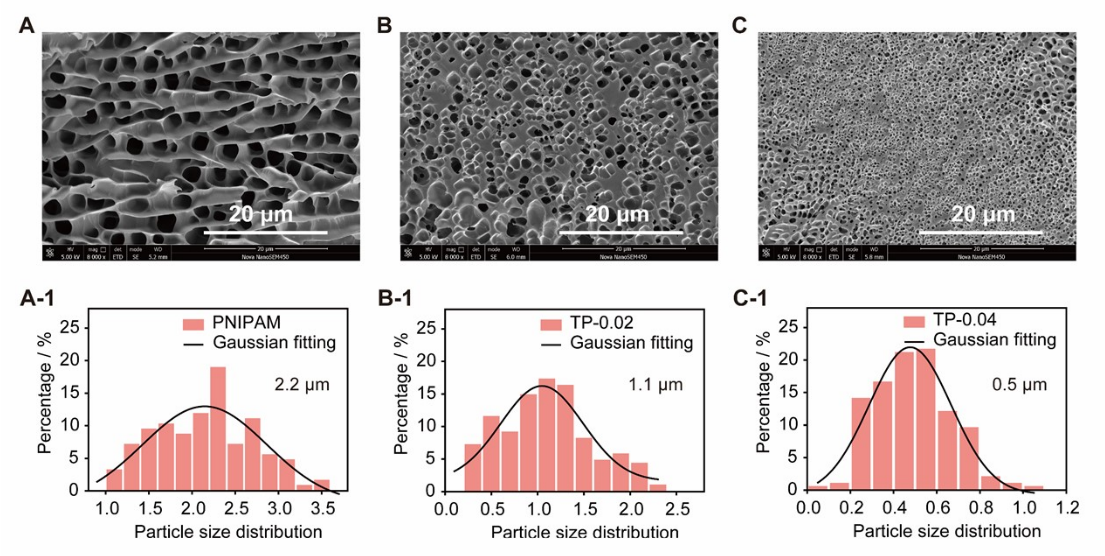

Fig. S4. The SEM (A-C) and the average pore size ((A-1)-(C-1)) of different samples after phase transition (A, A-1) PNIPAM, (B, B-1) TP-0.02 and (C, C-1) TP-0.04.

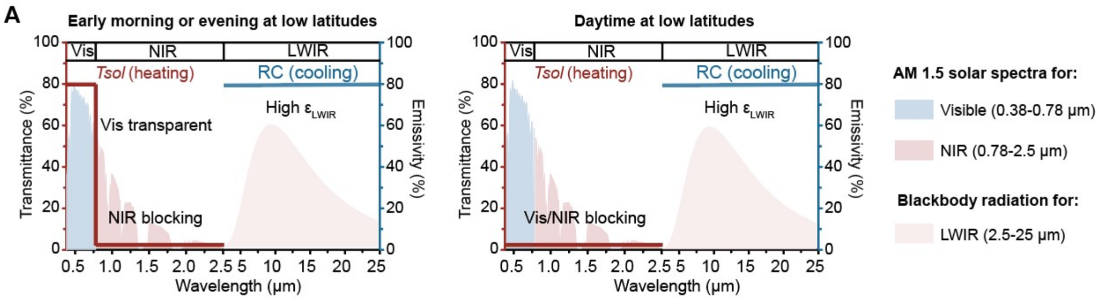

Fig. S5. Concept of the ideal energy-saving smart window at low latitudes.

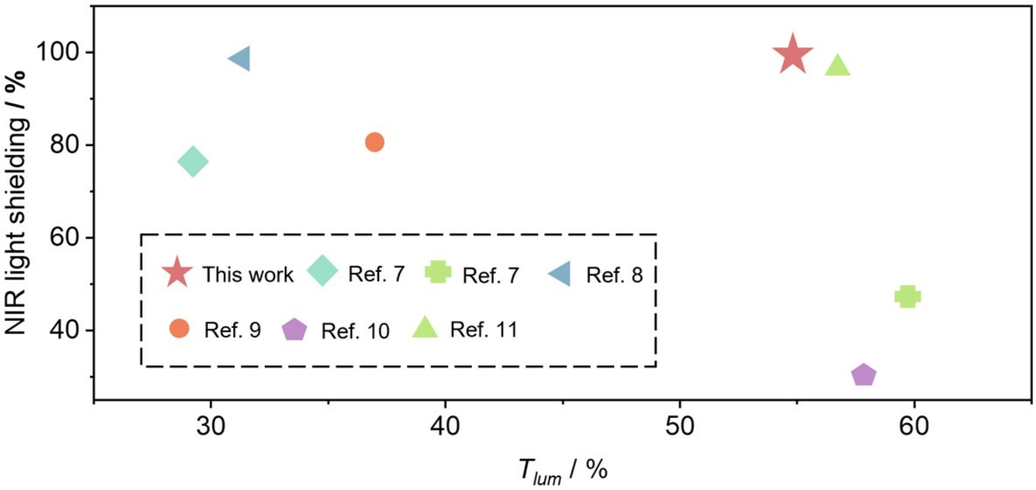

Fig. S6. Thermochromic performance (NIR light shielding and T_{lum}) in some of the best-reported smart materials[7-11].

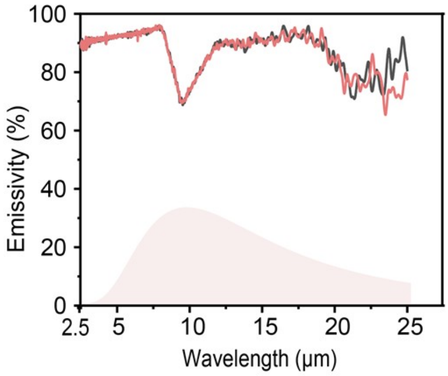

Fig. S7. LWIR emissivity curves of TP-0.04-PT smart window at different temperatures.

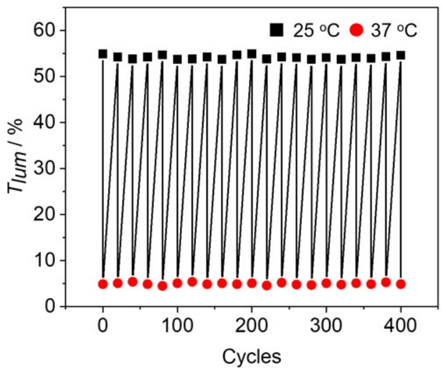

Fig. S8. The visible light transmittance (T_{lum}) at 25 ℃ (Black) and 37 ℃ (Red) measured after every 20 heating-cooling cycles.

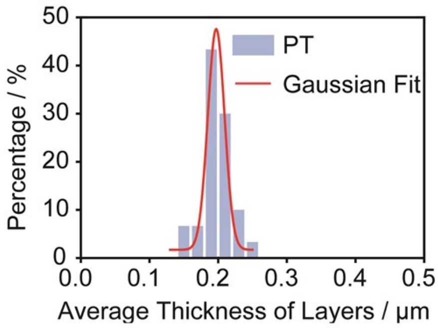

Fig. S9. Statistical analysis of average monolayer thickness (d) of photothermal film (PT film) (The difference between d_h and d_l is not significant, so it is assumed that $d = d_h = d_l$.).

The one-dimensional photonic crystal structure is a periodic nanostructure with a refractive index distribution along one direction, resulting in the elegant optical property called photonic band gap, which is defined as a waveband prohibiting light propagation. In general, artificial one-dimensional photonic crystals consist of two alternating materials. The calculation methods for the photonic band gap position (λ_{Bragg}) and stop band width (W) are given by Equations S9 and S10, respectively.

$$m\lambda_{Bragg} = 2D\sqrt{n_{eff}^2 - sin^2\Theta} \tag{9}$$

$$W = \frac{4}{\pi}\left|\frac{n_h - n_l}{n_h + n_l}\right| \tag{10}$$

$$D = d_h + d_l \tag{11}$$

$$n_{eff} = (n_h d_h + n_l d_l)/(d_h + d_l) \tag{12}$$

m is the diffraction order, λ_{Bragg} is the reflected light wavelength (photonic band gap position), D is the total of the thicknesses of the two adjacent layers, about 380 nm (Fig. S9), n_{eff} is the effective refractive index of the photonic crystal film, Θ is the incidence angle measured from the normal, W is the stop band width, d_h and d_l are the thicknesses of the two constituent layers, respectively, n_h and n_l are the refractive index of the two layers, respectively.

From Equations S9 and S10, it is evident that the theoretical λ_{Bragg} and W can be calculated when the values for the layer thickness (d_h and d_l) and refractive index (n_h and n_l) of the one-dimensional photonic crystal structure are known. By analyzing the cross-sectional SEM of the photo-thermal films, we can calculate the average layer thickness (d) of the one-dimensional photonic crystal structure (Fig. S9) (Assuming $d = d_h = d_l$). However, the refractive index of each layer cannot be fully determined, thus we cannot accurately calculate the theoretical λ_{Bragg} and W. Fortunately, the photonic crystal structure with a λ_{Bragg} of approximately 1050 nm and W of around 300 nm can be achieved theoretically through methods such as designing a gradient in layer thickness or controlling the refractive index difference between layers.

Actually, the photothermal films are commercially available products that consist of an alternate stacked structure and surface photo-thermal components as indicated by SEM (Fig. 3A) and EDS (Fig. 3B) analyses. Moreover, this alternating laminated structure can selectively reflect light in the 850-1150 nm range and exhibits the characteristics of a one-dimensional photonic crystal (Fig. 3D). Therefore, the mechanism of photothermal thin films can be understood from the fact that photonic crystal structures selectively reflect light in the 850-1150 nm range toward the photothermal component, thereby enhancing the efficiency of photothermal generation.

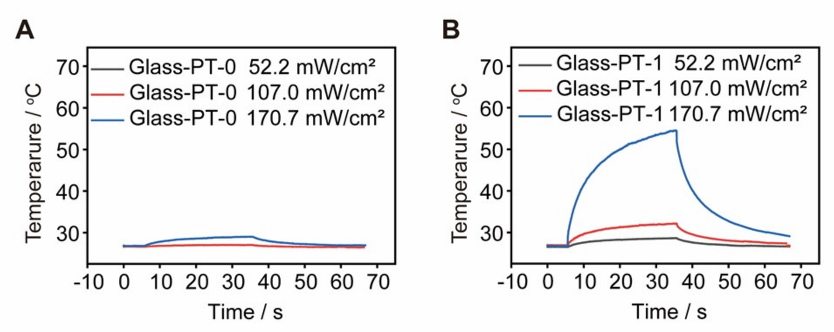

Fig. S10. The temperature change of different molds. "-0" and "-1" represent different surfaces of the photothermal film, respectively. "-0" represent the direction of the photonic crystal layer. "-1" represent direction of the photothermal coating.

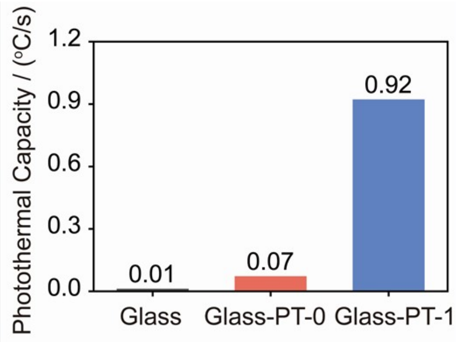

Fig. S11. The near-infrared (NIR) photothermal capability of Glass and Glass-PT molds. "-0" and "-1" represent different surfaces of the photothermal film, respectively. "-0" represent the direction of the photonic crystal layer. "-1" represent direction of the photothermal coating.

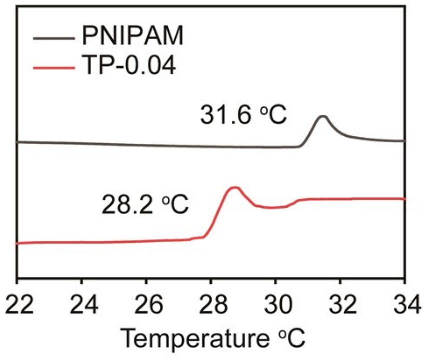

Fig. S12. DSC heating curves of PNIPAM gel.

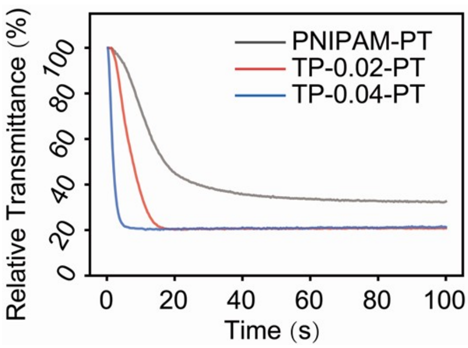

Fig. S13. The relative transmittance (550 nm) of hydrogel panels at 980 nm laser (170.7 mW/cm^2) response.

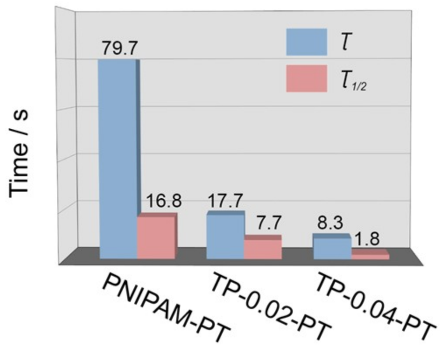

Fig. S14. The response speed of different smart hydrogel panels to 980 nm laser (170.7 mW/cm^2).

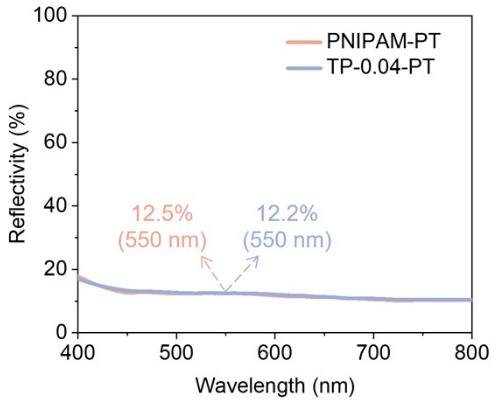

Fig. S15. The reflectivity (25 ℃) of the hydrogel panels (380-780 nm).

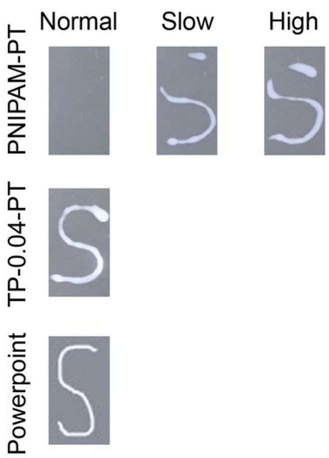

Fig. S16. Digital photos of different writing styles (-Normal (1.5 s/Byte, 640.1 mW/cm^2), -Slow (6.0 s/Byte, 640.1 mW/cm^2), -High (1.5 s/Byte, 853.8 mW/cm^2)).

The real-time image of the hydrogel panels was captured using a digital camera (Fig. S16). White (RGB: 255, 255, 255) lines were used to write the same letters in Microsoft PowerPoint using the color of the hydrogel panel image (RGB: 139, 143, 153) as the background, and the colored image was captured using the screenshot function of the Windows operating system. To quantitatively compare the clarity of the two writing methods, the RGB values in the image were converted to grayscale values using Equation S13.

A higher number of grayscale values indicates greater color richness in the image, while a larger difference in grayscale values corresponds to higher contrast and greater clarity of the writing. The clarity of writing in the two methods was quantitatively compared using the Brenner gradient ($D(f)$) and the sharpness difference between light and dark regions ($D(i)$) (Equation S14 and S17). The former reflects the cumulative difference in pixel grayscale values between adjacent pixels, while the latter indicates the difference in the average pixel grayscale values between the writing and non-writing regions. Therefore, higher values of $D(f)$ and $D(i)$ can indicate clearer writing results.

$$f(x,y) = 0.299R(x,y) + 0.587G(x,y) + 0.114B(x,y) \tag{13}$$

$$D(f) = \sum_{y}\sum_{x}|f(x+2,y) - f(x,y)|^2 \tag{14}$$

$$D_1 = \frac{1}{N_1}\sum_{x=1}^{N_x}\sum_{y=1}^{N_y} f_1(x,y) \tag{15}$$

$$D_2 = \frac{1}{N_2}\sum_{x=1}^{N_x}\sum_{y=1}^{N_y} f_2(x,y) \tag{16}$$

$$D(i) = D_1 - D_2 \tag{17}$$

The grayscale value ($f(x,y)$) of a pixel can be calculated from its red ($R(x,y)$), green ($G(x,y)$), and blue ($B(x,y)$) values. Brenner gradient ($D(f)$) is a fast edge detector which measures the difference between a pixel and its neighbor (Fig. S17). $D(i)$ is the difference in sharpness between light and dark (Fig. S18); D_1 and D_2 are the average grayscale values of the light and dark regions, respectively; $f_1(x,y)$ and $f_2(x,y)$ are the grayscale values of the light and dark regions, respectively; N_1 and N_2 are the number of grayscale points of the light region and dark region, respectively; X_D is the grayscale differentiation value of the light and dark regions. $X_D = 155$ was chosen to compare the writing clarity of different gel panels (Fig. 4E). The reason was that the writing background is uniform (PNIPAM-PT, $D(i)$=0) at this time.

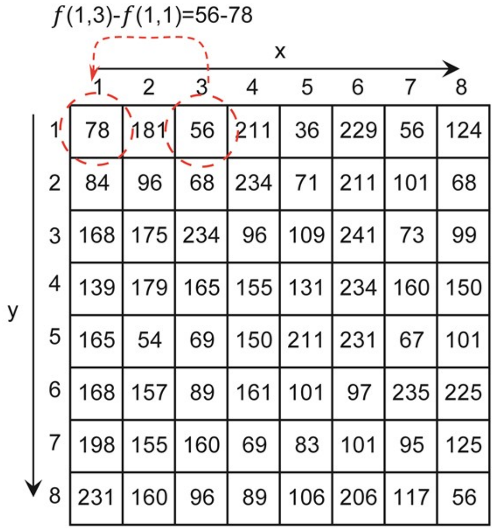

Fig. S17. Schematic diagram of the calculation of Brenner gradient ($D(f)$).

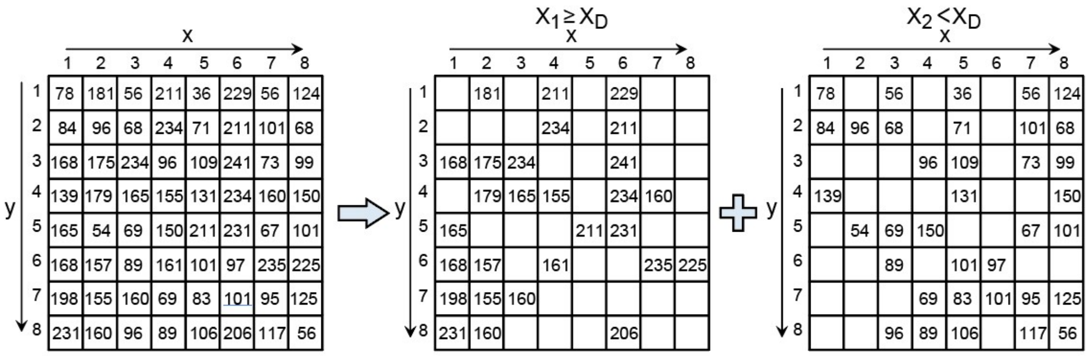

Fig. S18. Schematic diagram calculating sharpness difference between light and dark regions ($D(i)$).

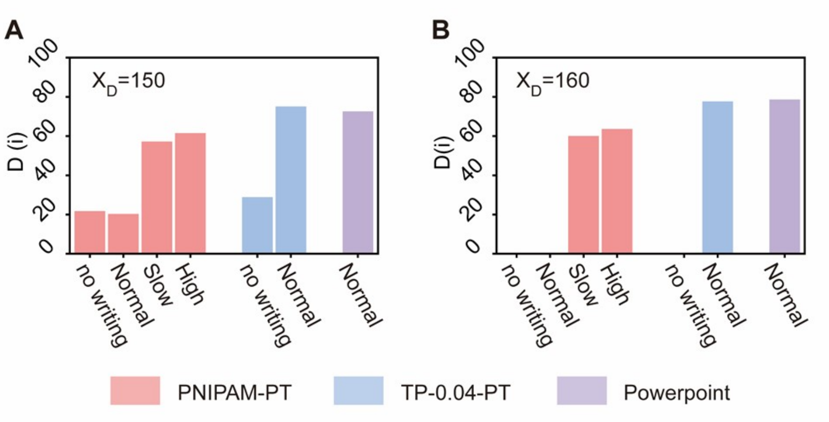

Fig. S19. The sharpness difference ($D(i)$) of the gel panels using the different X_D.

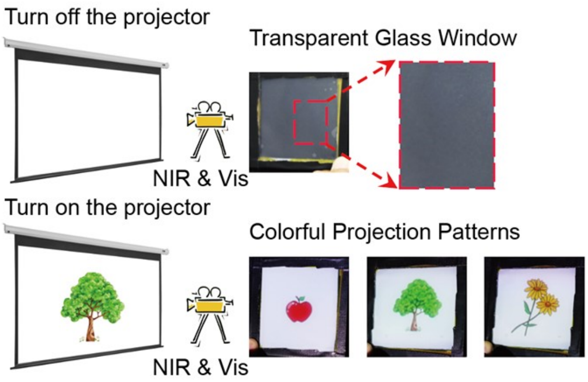

Fig. S20. Schematic diagrams and digital photos showing clear, colored images on smart windows.

Table S1. Optical properties for the samples used in building energy consumption simulation.

	Glass	**PNIPAM**	**PNIPAM-PT**	**TP-0.04-PT**
T_{sol} (%)	92.3 (25 °C)	81.4 (25 °C)	31.7 (25 °C)	31.8 (25 °C)
	92.3 (37 °C)	29.0 (37 °C)	5.3 (37 °C)	3.20 (37 °C)
R_{sol}, Front (%)	6.0 (25 °C)	6.4 (25 °C)	13.2 (25 °C)	12.9 (25 °C)
	6.0 (37 °C)	32.9 (37 °C)	33.8 (37 °C)	41.1 (37 °C)
R_{sol}, Back (%)	6.0 (25 °C)	6.4 (25 °C)	22.0 (25 °C)	24.4 (25 °C)
	6.0 (37 °C)	32.9 (37 °C)	27.5 (37 °C)	28.2 (37 °C)
T_{lum} (%)	89.8 (25 °C)	91.3 (25 °C)	54.8 (25 °C)	54.9 (25 °C)
	89.8 (37 °C)	15.6 (37 °C)	7.3 (37 °C)	4.9 (37 °C)
R_{lum}, Front (%)	7.1 (25 °C)	7.4 (25 °C)	12.2 (25 °C)	12.4 (25 °C)
	7.1 (37 °C)	46.0 (37 °C)	46.7 (37 °C)	53.5 (37 °C)
R_{lum}, Back (%)	7.1 (25 °C)	7.4 (25 °C)	9.0 (25 °C)	9.2 (25 °C)
	7.1 (37 °C)	46.0 (37 °C)	19.3 (37 °C)	19.4 (37 °C)
τC (°C)	--	32	32	28

Table S2. Thickness of the window components.

	Glass / (mm)	Gel / (mm)	TP / (mm)	Glass / (mm)
Glass	0.5	--	--	--
PNIPAM	0.5	0.5	--	0.5
PNIPAM-PT	0.5	0.5	0.075	0.5
TP-0.04-PT	0.5	0.5	0.075	0.5

Table S3. Thermochromic performance (NIR light shielding and T_{lum}) in some of the best-reported smart materials[7-11].

	T_{lum} / (%)	Near-infrared Light Shielding / (%)
This work	55	99
Ref. 7	30	76
	60	47
Ref. 8	31	99
Ref. 9	37	80
Ref. 10	58	30
Ref. 11	57	97

References

1. X.-H. Li, C. Liu, S.-P. Feng and N. X. Fang, *Joule*, 2019, **3**, 290-302.
2. S. Wang, T. Jiang, Y. Meng, R. Yang, G. Tan and Y. Long, *Science*, 2021, **374**, 1501-1504.
3. J. Liu, Y. Zhang, S. Li, C. Valenzuela, S. Shi, C. Jiang, S. Wu, L. Ye, L. Wang and Z. Zhou, *Chem. Eng. J.*, 2023, **453**, 139739.
4. S. Wang, Y. Zhou, T. Jiang, R. Yang, G. Tan and Y. Long, *Nano Energy*, 2021, **89**, 106440.
5. N. A. Lantonio and M. Krarti, *Appl. Energ.*, 2022, **328**, 120239.
6. W. Meng, A. J. J. Kragt, Y. Gao, E. Brembilla, X. Hu, J. S. van der Burgt, A. P. H. J. Schenning, T. Klein, G. Zhou, E. R. van den Ham, L. Tan, L. Li, J. Wang and L. Jiang, *Adv. Mater.*, 2024, **36**, 2304910.
7. S. Deng, Q. Chang, D. Li, B. Wang, H. Jin and J. Li, *ACS Appl. Energ. Mater.*, 2022, **5**, 3064-3071.
8. L. Zhang, Y. Du, H. Xia, F. xia, G. Yang and Y. Gao, *Ceram. Int.*, 2022, **48**, 37122-37131.
9. J. Chen, G. Li, T. Jiang, S. Wang, H. Hu, Z. Bai, D. Shi, M. Chen, J. Guan, G. Tan and Y. Long, *Nano Energy*, 2024, **123**, 109386.
10. L. Yang, W. Z. Xu, G. Moula and P. A. Charpentier, *Catal. Today*, 2023, **407**, 11-20.

11. L. Hu, C. Wang, H. Zhu, Y. Zhou, H. Li, L. Liu and L. Ma, *Small*, 2024, **20**, 2306823.